The Astrophysical Journal, 591:733–740, 2003 July 10
© 2003. The American Astronomical Society. All rights reserved. Printed in U.S.A.

TIMESCALES OF SOFT X-RAY VARIABILITY AND PHYSICAL CONSTRAINTS IN ACTIVE GALACTIC NUCLEI

W. Bian[1,2] and Y. Zhao[1]

Received 2002 July 18; accepted 2003 March 18

ABSTRACT

We present soft X-ray variability timescales for 65 active galactic nuclei (AGNs) derived from *ROSAT* Position Sensitive Proportional Counter pointing data. For these 65 objects with obvious exponential increasing or decreasing patterns in their light curves, we use the exponential timescales and find they are more suitable for analyzing *ROSAT* light-curve data. We also discuss some physical constraints on the central engine implied by our results. Assuming that this soft X-ray variability exponential timescale is approximately equal to the thermal timescale of the standard accretion disk, we obtain the accretion rate, the size of the soft X-ray radiation region, and the compactness parameter for 37 AGNs, using their recently estimated central black hole masses. For 12 of these 37 AGNs, the radii of the gravitational instability in the standard thin accretion disks are obtained using the central black hole masses and the calculated accretion rates. These are consistent with the results from the reverberation mapping method. These results provide supporting evidence that such gravitational instabilities contribute to the formation of the broad-line regions in AGNs.

Subject headings: accretion, accretion disks — galaxies: active — galaxies: nuclei — galaxies: Seyfert — quasars: general — X-rays: galaxies

1. INTRODUCTION

X-ray variability has long been known to be a common property of active galactic nuclei (AGNs). The X-ray variability in the continuum and in emission lines can give a clue to the central engine in AGNs (Mushotzky, Done, & Pounds 1993). The variance amplitude and the timescale are two main parameters that characterize the variance. There are many quantities that can be used to describe the variability amplitude or the timescale in X-ray variability, such as the flux-doubling timescale (Barr & Mushotzky 1986), normalized variability amplitude (Green, McHardy, & Lehto 1993), and the excess variance (Nandra et al. 1997). Some powerful methods are also introduced in the analysis of the X-ray light curves. These include the power density spectrum (PDS), the wavelet method (Otazu et al. 2002), and the power density in the time domain (Li 2001).

There has been steady progress on the analysis of X-ray variability since the launch of *EXOSAT*, the *Rossi X-Ray Timing Explorer* (*RXTE*), *ROSAT*, *ASCA*, and *XMM-Newton*. For an individual X-ray light curve, PDS analysis is now popular and can offer more information about the X-ray variability. Early attempts to constrain a PDS flattening or "cutoff," which relates to a characteristic timescale, were made with the *EXOSAT* data of NGC 5506 (McHardy 1988) and NGC 4151 (Papadakis & McHardy 1995). These analyses yield evidence for a cutoff timescale of several weeks. However, the uneven sampling of these data made their reliability uncertain. The situation was significantly improved with the launch of *RXTE*. Using *RXTE* data, Edelson & Nandra (1999) obtained an evenly sampled X-ray light curve of NGC 3516 and produced a PDS covering 4 decades in temporal frequency, finding a cutoff timescale of about 1 month. Pounds et al. (2001) also found a cutoff timescale of about 13 days for a narrow-line Seyfert 1 galaxy (NLS1; Ark 564). Uttley, McHardy, & Papadakis (2002) recently developed a Monte Carlo method to test models for the true power spectrum of intermittently sampled light curves against the observed noisy power spectra of four Seyfert galaxies, which are flat toward lower frequencies. They fitted two models for the flattening: a "knee" model and a "high-frequency break" model. They reduced the characteristic frequency for these four AGNs.

The X-ray characteristic timescale or frequency usually relates to the size of the X-ray emission region, which then can be used to constrain the central engine, e.g., the central black hole masses, accretion rates, and the radiation mechanism.

ROSAT observations of AGNs offer plenty of information about the soft X-ray variability, which is thought to come from the accretion disk around the central black hole in these AGNs. However, PDS analysis is not suitable for analyzing *ROSAT* pointed data, since there are usually large time gaps between adjacent exposures in *ROSAT* pointing observations. Thus, timescale analysis remains necessary in AGN samples. There are obvious exponentially increasing or decreasing patterns in the soft X-ray light curves in some AGNs observed with the *ROSAT* Position Sensitive Proportional Counter (PSPC) in pointing mode. In this paper we use the exponential timescale (Zhao & Fink 1996) to investigate the soft X-ray variability in AGNs with this kind of pattern. This paper is a continuation of the previous work of Zhao & Fink (1996).

The standard model of AGNs is an accretion disk with a jet around a central massive black hole. Progress on reliable estimates of black hole masses can effectively constrain the central engine when combined with research on the X-ray variability. Several methods have been used to estimate the mass of a black hole in the center of a galaxy. These include stellar dynamical studies (reviewed by Kormendy & Gebhardt 2001), reverberation mapping methods (Kaspi et al. 2000), analyses of the high-frequency tail of the PDS (Czerny et al. 2001), the relation between central black hole

[1] National Astronomical Observatories, Chinese Academy of Sciences, Beijing 100012, China.
[2] Department of Physics, Nanjing Normal University, Nanjing 210097, China.

masses and the bulge velocity dispersion, $M_{\rm BH}$-σ (Merritt & Ferrarese 2001), and the use of single-epoch rest-frame optical spectrophotometric measurements (Vestergaard 2002).

In § 2 timescales and central black hole masses of our sample are presented. We then give the physical constraints on the central engine of 37 AGNs in § 3. In § 4 we derive the radii of the gravitational instability in the standard α accretion disks of 12 AGNs and compare them with broad-line region (BLR) sizes from the reverberation mapping method. Our results are summarized in § 5. The cosmological parameters $H_0 = 75$ km s^{-1} Mpc^{-1} and $q_0 = 0.5$ have been adopted in this work.

2. THE SAMPLE AND TIMESCALES OF VARIABILITY

All sources were observed in *ROSAT*/PSPC mode over periods varying from days to years. We picked out the AGNs from cross-identification of the Véron-Cetty & Véron (2001) AGN catalog with the *ROSAT* point-source catalog. From the *ROSAT* public archive of PSPC observations, only sources with total X-ray photon counts greater than 1000 were selected to ensure the quality of the X-ray spectra. This yielded more than 200 AGNs. The data were processed for instrument corrections (such as vignetting and dead-time effects) and background-subtraction using the EXSAS/MIDAS software.

The light curve for each AGN was obtained from original *ROSAT* observations with a 400 s time bin in three energy bands: 0.1–2.4 (total band), 0.1–0.4 (*A* band), and 0.5–2.0 (*B* band) keV. The estimates of timescales for all AGNs described below are based on those light curves. From these light curves we can find that there exist obvious exponentially increasing or decreasing patterns. Since X-ray emission is believed to come from the accretion disk around the central black hole in AGNs, these exponential patterns may provide physical insight. We select the AGN light curves with exponential patterns by the following criteria: (1) The count rate increases or decays continually in the light curves, considering count rate uncertainties of 3 σ. (2) The number of contiguous data points fitted by the exponential function (eq. [1]) is greater than 4. (3) The magnitude of the count rate variance is greater than $5[(\sigma_1^2 + \sigma_2^2)]^{1/2}$, where σ_1 and σ_2 are the count rate errors of the jumping-off point and endpoint, respectively. The soft X-ray luminosity in the 0.1–2.4 keV band of each AGN is obtained by averaging the power-law–fitting spectra of all the observations.

2.1. *Exponential Timescales*

We use the exponential timescale (Zhao & Fink 1996) to characterize the exponential pattern in the light curves in AGNs. The exponential timescale, Δt_e, is defined as

$$I(t) = I_0 + I_a e^{\pm t/\Delta t_e} , \qquad (1)$$

where $I(t)$ is the count rate at t and I_0 and I_a are constants.

The definition of the exponential timescale is based on instabilities that increase or decrease exponentially. Thus, the exponential timescale is equivalent to a rising or a descending timescale, and I_a is the amplitude of variability. The quantity I_0 is an additional constant component, which is equal to the intensity before or after the instability. It is exponentially increasing if the sign of I_a is positive, while it is exponentially decaying if the sign is negative. For AGNs with more than one value of Δt_e, we select Δt_e with the smallest error as the timescale. Taking the Seyfert 1 galaxy (S1) NGC 5548 as an example (Fig. 1), there are three obvious exponentially increasing or decreasing patterns in the light curve. Three patterns fitted by equation (1) showed similar exponential timescales. The exponential timescales are $(1.04 \pm 0.32) \times 10^5$, $(6.65 \pm 5.35) \times 10^4$, and $(8.17 \pm 0.26) \times 10^4$ s, which are consistent if taking the errors into account, and I_0 is 3.10 ± 0.13, 7.16 ± 0.87, and 6.01 ± 0.10 photons s^{-1}, respectively.

We think there is more physical information in the exponential timescale than in the two-folding timescale, which considers the amplitude being increased by only a factor of 2. There are usually large time gaps between adjacent exposures in *ROSAT* pointed observations. The two-folding timescale overestimates the timescale of *ROSAT* sources. Using our selection criteria as defined above, we searched for any obvious continually exponentially increasing or decreasing pattern in the light curve of each AGN and then fitted the pattern with the form of equation (1), considering the errors of the count rates (Press 1992). The exponential timescales for 65 AGNs are listed in column (3) of Table 1, in which there are nine quasars (QSOs), 37 S1s, nine NLS1s, one Seyfert 2 galaxy (S2), four BL Lac objects (BLs), and five high optical polarization (HP) objects. The timescales calculated as rising exponentials are marked with an asterisk. The rest are derived from decaying exponentials.

2.2. *Estimations of Central Black Hole Masses*

The masses of the 13 AGNs from reference 1 in Table 1 are adopted from Nelson (2000). They were estimated from reverberation mapping methods with a high level of reliability. There is strong correlation between the black hole mass and the host velocity dispersion, namely, the $M_{\rm BH}$-σ relation (Ferrarese et al. 2001). We adopt the $M_{\rm BH}$-σ relation found by Merritt & Ferrarese (2001), namely,

$$M_{\rm BH} = 1.3 \times 10^8 \ M_\odot \left(\frac{\sigma}{200 \text{ km s}^{-1}} \right)^{4.72} . \qquad (2)$$

We derive masses for seven AGNs with measured host velocity dispersions, which are from reference 6 in Table 1 (Nelson & Whittle 1995; Falomo, Kotilainen, & Treves 2002). The errors for the black hole masses in these seven AGNs are estimated from the errors of the bulge velocity dispersion. An empirical relationship between single-epoch rest-frame optical spectrophotometric measurements and the central masses was recently presented (Vestergaard 2002). These methods for estimating AGN masses are all calibrated using masses from the reverberation mapping method. The total number of AGNs with available black hole masses is 37, of which there are 22 S1s, five NLS1s, one S2, eight QSOs, and one BL. The central black hole masses of these 37 AGNs are listed in column (5) of Table 1.

3. ANALYSIS AND PHYSICAL CONSTRAINTS

3.1. *Central Black Hole Mass and Mass Limits from the Exponential Timescale*

The upper limit on the mass of the central black hole in AGNs derived from the timescale is defined as (Mushotzky et al. 1993)

$$M(\Delta t) = 2 \times 10^4 \left(\frac{\Delta t}{1 \text{ s}} \right) \ M_\odot , \qquad (3)$$

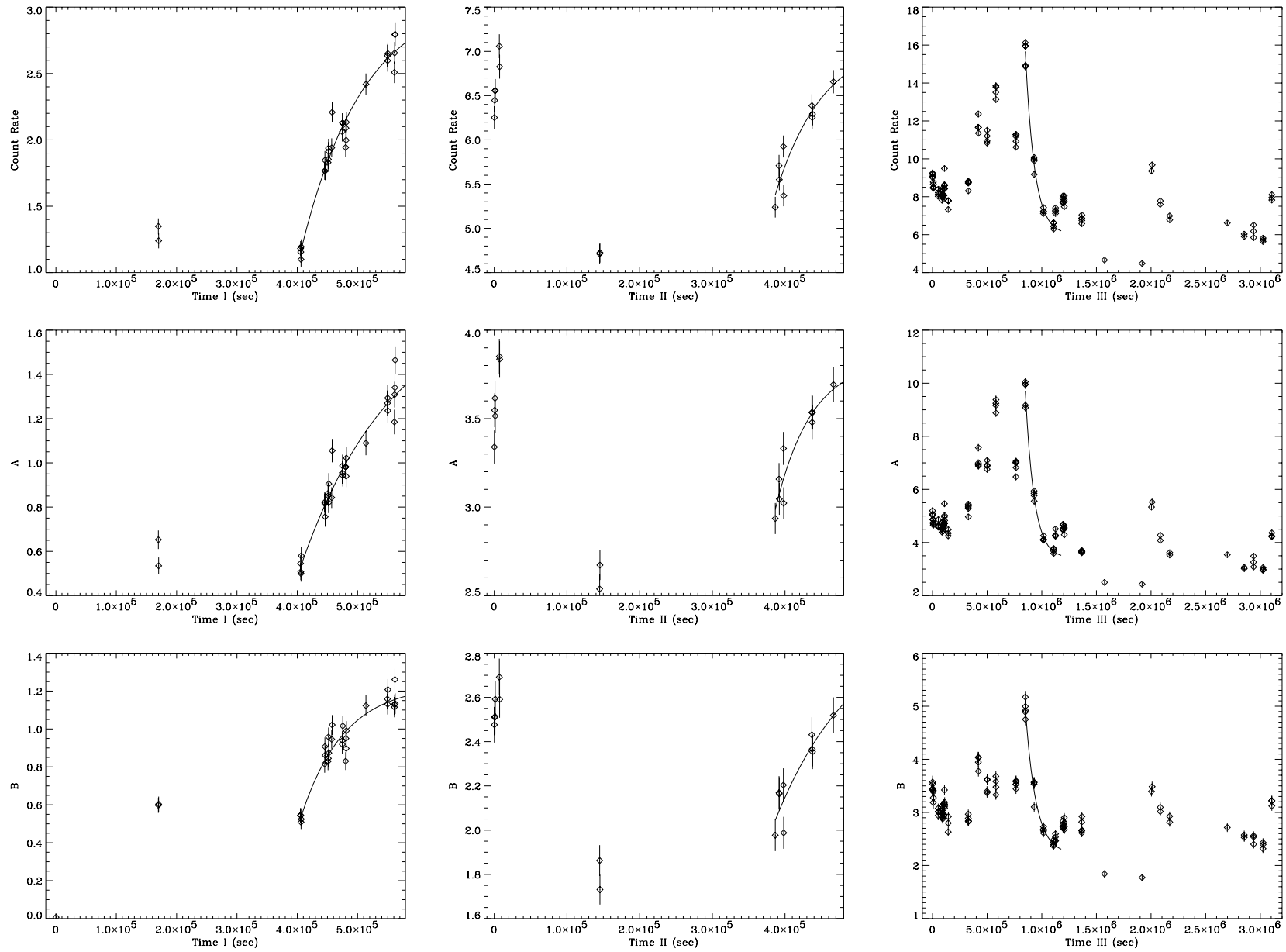


FIG. 1.—Variability of the count rate and exponential timescale fitting of NGC 5548 in three energy bands: 0.1–2.4 (total band), 0.1–0.4 (*A* band), and 0.5–2.0 (*B* band) keV. The time zero is at 22:48:59 UT on 1990 July 18 for time I, at 23:19:29 UT on 1992 January 17 for time II, and at 9:23:14 UT on 1992 December 24 for time III.

TABLE 1

PROPERTIES OF 65 AGNs IN RIGHT ASCENSION ORDER

Name (1)	Type (2)	ΔT_e (10^4 s) (3)	L_X (10^{43} ergs s^{-1}) (4)	$\log(M/M_\odot)$ ($M_\odot$) (5)	$\log \dot{M}$ ($M_\odot$ yr^{-1}) (6)	$\log(R_X/R_g)$ (7)	$\log(l)$ (8)	References (9)
Mrk 335	S1	7.45 ± 3.05	27.7 ± 1.5	$6.8^{+0.14}_{-0.14}$	$0.011^{+0.31}_{-0.31}$	$1.95^{+0.29}_{-0.29}$	$1.30^{+0.34}_{-0.34}$	1
I Zw 1	NLS1	0.279 ± 0.302	93 ± 17.3	$7.21^{+0.1}_{-0.1}$	$-0.69^{+0.43}_{-0.43}$	$0.73^{+0.10}_{-0.10}$	$2.64^{+0.44}_{-0.44}$	2
Ton S 180	NLS1	0.201 ± 0.140*	99.4 ± 6.5	$8.16^{+0.5}_{-0.5}$	$-1.39^{+0.59}_{-0.59}$	$-1.3\mathrm{E}-5^{+0.57}_{-0.57}$	$2.44^{+0.77}_{-0.77}$	3
F9	S1	1.69 ± 0.50	79.9 ± 3.9	$7.9^{+0.11}_{-0.31}$	$-0.69^{+0.24}_{-0.30}$	$0.79^{+0.21}_{-0.29}$	$1.82^{+0.261}_{-0.44}$	1
PHL 1092	NLS1	8.84 ± 4.60	2870 ± 1190	$6.09^{+0.5}_{-0.5}$	$2.54^{+1.05}_{-1.05}$	$2.48^{+0.48}_{-0.48}$	$3.50^{+1.16}_{-1.16}$	4
MS 01585+0019	BL	0.0529 ± 0.0748*	274 ± 57	...	...	...	...	...
Mrk 586	QSO	0.806 ± 1.124	317 ± 45	$7.75^{+0.64}_{-0.30}$	$-0.21^{+1.08}_{-1.01}$	$0.68^{+1.02}_{-0.95}$	$2.69^{+1.25}_{-1.05}$	5
ESO 198-G24	S1	1.58 ± 0.74*	26.3 ± 1.4	...	...	...	...	...
Mrk 372	S1	8.11 ± 12.37	4.11 ± 0.60	...	...	...	...	...
NGC 1275	S1.5	0.08 ± 0.122*	63 ± 19.1	$8.55^{+0.32}_{-0.32}$	$-2.11^{+1.23}_{-1.23}$	$-0.53^{+1.02}_{-1.02}$	$2.39^{+1.27}_{-1.27}$	6
NGC 1566	S1	25.2 ± 14.8	0.0278 ± 0.0036	$6.69^{+0.47}_{-0.47}$	$-2.56^{+0.58}_{-0.58}$	$2.38^{+0.50}_{-0.50}$	$-2.01^{+0.745}_{-0.75}$	6
Ark 120	S1	0.204 ± 0.152	36.4 ± 2.2	$8.26^{+0.08}_{-0.12}$	$-1.89^{+0.52}_{-0.52}$	$-0.06^{+0.50}_{-0.50}$	$1.97^{+0.52}_{-0.53}$	1
PKS 0548−322	HP	0.0745 ± 0.1561	150 ± 5	...	...	...	...	...
S5 0716+71	HP	0.147 ± 0.052*	...	...	...	...	...	...
MS 07379+7441	BL	2.69 ± 2.60*	861 ± 95	...	...	...	...	...
Mrk 10	S1	0.0596 ± 0.0438	10.4 ± 1.2	$7.34^{+1.31}_{-1.31}$	$-2.17^{+1.04}_{-1.04}$	$0.19^{+1.00}_{-1.00}$	$2.09^{+1.67}_{-1.67}$	6
VII Zw 244	S1	1.12 ± 0.52*	62.7 ± 18.9	...	...	...	...	...
ESO 434-G40	S1	0.102 ± 0.083	0.715 ± 0.806	7.58^{+1}_{-1}	$-3.34^{+2.68}_{-2.68}$	$0.19^{+0.86}_{-0.86}$	$0.69^{+2.868}_{-2.86}$	7
NGC 3031 (M81)	S1	6.82 ± 0.86	...	$7.83^{+0.04}_{-0.09}$	$-2.14^{+0.24}_{-0.25}$	$1.24^{+0.09}_{-0.10}$	$-0.46^{+0.24}_{-0.26}$	8
IRAS 09595−075	S1	41.0 ± 14.4	13.1 ± 1.4	...	...	...	...	...
HE 1029−1401	QSO	4.73 ± 3.39	236 ± 12	...	...	...	...	...
MS 10590+7302	S1	0.904 ± 0.889*	18.7 ± 2.7	...	...	...	...	...
NGC 3516	S1	2.46 ± 0.99	3.17 ± 0.1	$7.36^{+0.12}_{-0.12}$	$-1.62^{+0.29}_{-0.29}$	$1.26^{+0.28}_{-0.27}$	$0.49^{+0.31}_{-0.31}$	1
Mrk 180	BL	0.112 ± 0.221	36.2 ± 5.3	$8.55^{+0.19}_{-0.19}$	$-2.25^{+1.37}_{-1.37}$	$-0.43^{+1.32}_{-1.32}$	$2.05^{+1.38}_{-1.38}$	6
NGC 3783	S1	0.756 ± 2.806	2.15 ± 0.45	$6.97^{+0.30}_{-0.97}$	$-1.87^{+2.54}_{-2.61}$	$1.18^{+2.48}_{-2.56}$	$0.80^{+2.344}_{-2.78}$	1
Mrk 1310	S1	0.529 ± 0.366*	0.451 ± 0.06	...	...	...	...	...
NGC 4051	NLS1	0.684 ± 0.05*	0.0651 ± 0.003	$6.11^{+0.30}_{-0.41}$	$-2.85^{+0.23}_{-0.30}$	$1.72^{+0.21}_{-0.27}$	$-0.4^{+0.38}_{-0.51}$	1
GQ COM	QSO	0.0713 ± 0.0575	72.4 ± 7.1	...	...	...	...	...
NGC 4151	S1	0.0784 ± 0.0461	0.0472 ± 0.0031	$7.18^{+0.23}_{-0.38}$	$-4.33^{+0.44}_{-0.49}$	$0.38^{+0.42}_{-0.46}$	$-0.2^{+0.50}_{-0.62}$	1
PG 1211+143	QSO	30.2 ± 10.6*	139 ± 17	$7.61^{+0.09}_{-0.15}$	$0.577^{+0.37}_{-0.38}$	$1.82^{+0.24}_{-0.24}$	$1.32^{+0.38}_{-0.40}$	...
B2 1215+30	HP	10.4 ± 4.6	...	...	...	...	...	...
Mrk 766	S1	0.165 ± 0.045*	2.52 ± 0.09	$6.63^{+0.5}_{-0.5}$	$-2.02^{+0.39}_{-0.39}$	$0.96^{+0.38}_{-0.38}$	$1.42^{+0.63}_{-0.63}$	3
PG 1307+085	QSO	9.19 ± 5.03	122 ± 22	$8.45^{+0.14}_{-0.45}$	$-0.38^{+0.35}_{-0.62}$	$0.91^{+0.38}_{-0.47}$	$1.33^{+0.37}_{-0.77}$	1
PG 1218+304	HP	6.61 ± 2.21	...	...	...	...	...	...
B2 1223+25	QSO	24.3 ± 15.1	65.9 ± 15	8.66	$-0.51^{+0.94}_{-0.94}$	$1.05^{+0.78}_{-0.78}$	$0.71^{+1.37}_{-1.37}$	7
3C 273.0	QSO	16.9 ± 4.9*	1220 ± 20	$8.74^{+0.07}_{-0.07}$	$0.60^{+0.20}_{-0.20}$	$0.90^{+0.20}_{-0.20}$	$2.06^{+0.21}_{-0.21}$	1
Ton 1542	S1	22.2 ± 7.6	41.2 ± 3.9	$7.88^{+0.17}_{-0.27}$	$-0.22^{+0.33}_{-0.36}$	$1.55^{+0.25}_{-0.29}$	$0.80^{+0.37}_{-0.45}$	1
NGC 4579	S1.9	1.45 ± 0.96*	0.163 ± 0.015	$7.78^{+0.5}_{-0.5}$	$-3.34^{+0.59}_{-0.59}$	$0.83^{+0.55}_{-0.55}$	$-0.78^{+0.77}_{-0.77}$	6
Was 61	NLS1	10.8 ± 0.44*	12.4 ± 1.8	...	...	...	...	...
PG 1244+026	NLS1	0.0130 ± 0.0328	54.1 ± 11.5	$6.11^{+0.5}_{-0.5}$	$-1.08^{+1.79}_{-1.79}$	$0.57^{+1.71}_{-1.71}$	$3.66^{+1.84}_{-1.85}$	3
MS 12480−0600A	S1	0.222 ± 0.714	110 ± 19	...	...	...	...	...
K07.01	S1	1.33 ± 1.19*	31.8 ± 9.1	...	...	...	...	...
NGC 5033	S1.9	0.251 ± 0.122*	0.0274 ± 0.0024	5.9^{+1}_{-1}	$-3.38^{+0.76}_{-0.76}$	$1.57^{+0.73}_{-0.73}$	$-0.4^{+1.25}_{-1.25}$	7
K08.02	S1	0.0557 ± 0.0354*	13.1 ± 2.2	...	...	...	...	...
MS 13326−2935	BL	4.39 ± 2.45	87.2 ± 15.3	...	...	...	...	...
MCG +06-30-015	S1	0.855 ± 0.197	1.10 ± 0.06	$5.94^{+0.5}_{-0.5}$	$-1.44^{+0.39}_{-0.39}$	$1.90^{+0.37}_{-0.37}$	$0.81^{+0.632}_{-0.63}$	4
IRAS 13349+243	QSO	559 ± 118	82.8 ± 15.2	...	...	...	...	...
2E 1346+2646	NLS1	19 ± 5.8*	4.53 ± 0.65	...	...	...	...	...
NGC 5548	S1	8.17 ± 0.26*	4.47 ± 0.08	$8.09^{+0.07}_{-0.07}$	$-1.61^{+0.07}_{-0.07}$	$1.12^{+0.05}_{-0.05}$	$0.05^{+0.10}_{-0.10}$	1
PG 1416−129	S1.2	41.5 ± 35.5	99 ± 14.7	$8.40^{+0.12}_{-0.12}$	$-0.01^{+0.66}_{-0.67}$	$1.38^{+0.57}_{-0.57}$	$0.82^{+0.67}_{-0.67}$	2
Mrk 474	S1	1.54 ± 0.66*	13.6 ± 1	...	...	...	...	...
Mrk 841	S1	7.05 ± 2.81	23.3 ± 1	8.3	$-1.08^{+0.73}_{-0.73}$	$0.94^{+0.72}_{-0.72}$	$0.74^{+1.23}_{-1.23}$	...
Mrk 290	S1	8.86 ± 29.24*	4.64 ± 0.57	$7.50^{+0.12}_{-0.12}$	$-1.18^{+2.23}_{-2.23}$	$1.54^{+2.20}_{-2.20}$	$0.24^{+2.22}_{-2.22}$	2
Mrk 876	QSO	139 ± 88.3*	109 ± 12	$8.38^{+0.18}_{-0.20}$	$0.40^{+4.27}_{-4.27}$	$1.75^{+4.24}_{-4.23}$	$0.52^{+4.25}_{-4.25}$	1
NGC 6251	S2	5.69 ± 8.55*	1.58 ± 1.21	$8.78^{+0.12}_{-0.48}$	$-2.63^{+2.00}_{-2.02}$	$0.55^{+1.00}_{-1.05}$	$-0.53^{+2.00}_{-2.07}$	8
3C 345.0	HP	2260 ± 1180*	644 ± 51	...	...	...	...	...
EXO 1652.4+393	NLS1	0.075 ± 0.0567*	9.18 ± 3.28	...	...	...	...	...
NGC 6814	S1.5	1.62 ± 0.91	0.0758 ± 0.015	$6.98^{+0.74}_{-0.74}$	$-3.11^{+0.77}_{-0.77}$	$1.39^{+0.62}_{-0.62}$	$-0.88^{+1.06}_{-1.06}$	6
F339	S1	6.12 ± 2.54	81.2 ± 18.4	...	...	...	...	...
NGC 7214	S1	1.61 ± 0.76*	7.35 ± 0.38	...	...	...	...	...
NGC 7213	S1	3.53 ± 2.47*	1.15 ± 0.03	$7.95^{+0.51}_{-0.51}$	$-2.35^{+0.58}_{-0.58}$	$0.97^{+0.58}_{-0.58}$	$-0.25^{+0.772}_{-0.77}$	6
MS 22549−3712	S1	0.341 ± 0.293	16.5 ± 3.6	...	...	...	...	...
NGC 7469	S1	4.99 ± 0.40*	7.63 ± 0.28	$6.81^{+0.30}_{-3.81}$	$-0.67^{+0.22}_{-2.55}$	$1.83^{+0.21}_{-2.54}$	$0.85^{+0.37}_{-4.58}$	1
Mrk 926	S1.5	0.172 ± 0.419*	78.6 ± 4.5	8.46^{+1}_{-1}	$-1.73^{+1.77}_{-1.77}$	$-0.2^{+1.76}_{-1.76}$	$2.29^{+2.02}_{-2.02}$	7
MS 23409−1511	NLS1	0.126 ± 0.192	249 ± 32	...	...	...	...	...

NOTES.—Col. (1): Name. Col. (2): Type. Col. (3): Exponential timescale. Col. (4): Luminosity at 0.1–2.4 keV. Col. (5): log of the BH mass. Col. (6): log of the calculated accretion rates. Col. (7): log of the ratio of the size of the X-ray emission region to the Schwarzschild radius. Col. (8): log of the compactness parameter. An asterisk denotes an exponential timescale from the rising variation. References are the sources of the estimates of the central black hole mass.

REFERENCES.—(1) Nelson 2000; (2) Vestergaard 2002; (3) Wang & Lu 2001; (4) Czerny et al. 2001; (5) Mathur, Kuraszkiewicz, & Czerny 2001; (6) Nelson & Whittle 1995; Falomo et al. 2002; (7) Padovani, Burg, & Edelson 1990; (8) Tremaine et al. 2002.

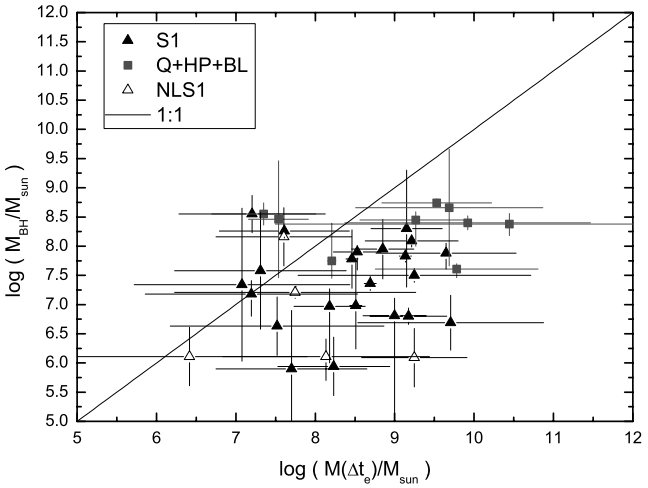


FIG. 2.—Black hole masses vs. the mass limits derived from the exponential timescales. The solid line shows 1 : 1.

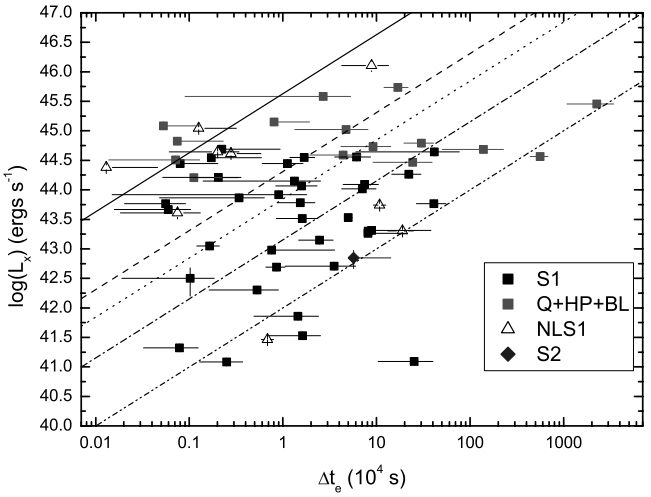


FIG. 3.—Soft X-ray luminosity vs. exponential timescales, with the Eddington limit (*solid line*), efficiency limit ($\eta = 0.1$; *dashed line*), compact parameter limit ($l = 60$; *dotted line*), efficiency limit ($\eta = 0.007$; *dot-dashed line*), and bremsstrahlung limit (*double-dot–dashed line*), assuming $L_{\rm bol} = 10L_{\rm X}$.

assuming that the size of the X-ray radiation region is 5 Schwarzschild radii.

We compared this mass limit derived from the exponential timescales with the above estimated central black hole masses (see § 2.2) in Figure 2. This shows that the exponential timescale can also provide an effective limit for the mass of a central black hole in an AGN.

3.2. *Constraints on the Radiation Mechanism in AGNs*

Some physical constraints on the relationship of bolometric luminosity and the timescale were proposed by Fabian (1979, 1992). If the source luminosity is below the Eddington limit, we obtain a limit

$$L_{\rm bol} \leq \frac{2}{3}\pi\frac{m_p c^4}{\sigma_{\rm T}}\Delta t \text{ ergs s}^{-1} . \quad (4)$$

When the luminosity is produced by matter energy being transformed into radiation with some efficiency $\eta \ll 1$, there is a second limit:

$$L_{\rm bol} \leq \eta\frac{m_p c^4}{\sigma_{\rm T}}\Delta t \text{ ergs s}^{-1} . \quad (5)$$

If the primary spectrum of the source extends to γ-ray energies, electron-positron pair production gives a third limit:

$$L_{\rm bol} \leq 20\pi\frac{m_e c^4}{\sigma_{\rm T}}\Delta t \text{ ergs s}^{-1} . \quad (6)$$

Thermal bremsstrahlung radiation supplies more power than the Compton process only if

$$L_{\rm bol} \leq 10^{39} T_9^{-3/2}\Delta t \text{ ergs s}^{-1} , \quad (7)$$

where the temperature of the electrons is $T_9 10^9$ K.

The bolometric luminosity is larger than the X-ray luminosity in *ROSAT*'s energy band. For example, the ratio of the bolometric luminosity of 3C 273 (Padovani & Rafanelli 1988), 1.7×10^{47} ergs s^{-1}, and the X-ray luminosity in *ROSAT*'s energy band, 1.2×10^{46} ergs s^{-1}, is 14. In Figure 3 we show the soft X-ray luminosity in the 0.1–2.4 keV band versus the exponential timescale. The lines in Figure 3 are from equations (4)–(7), assuming $L_{\rm bol} = 10L_{\rm X}$.

From Figure 3 bremsstrahlung is ruled out as the primary radiation source except in several low-luminosity sources because of the observed rapid variability.

The objects whose bolometric luminosities are larger than the Eddington limit are MS 01585+0019 (BL), PKS 0548−322 (HP), MS 23409−1511 (NLS1), and PG 1244+026 (NLS1). These objects may display relativistic effects.

The efficiency factors η of most objects are larger than 0.007, which would not be associated with stellar process (see Fig. 3). It suggests strongly that most AGNs, at least, have nonthermal and nonstellar processes that are produced by a very efficient central engine.

We also plot $L_{\rm X}$ versus central black hole mass in Figure 4. The solid line shows $L_{\rm X} = 0.1L_{\rm Edd}$, and the dashed line shows $L_{\rm X} = 10^{-4}L_{\rm Edd}$. If we assume $L_{\rm bol} = 10L_{\rm X}$, we find that the efficiency factor is between 1 and 10^{-3}, which is

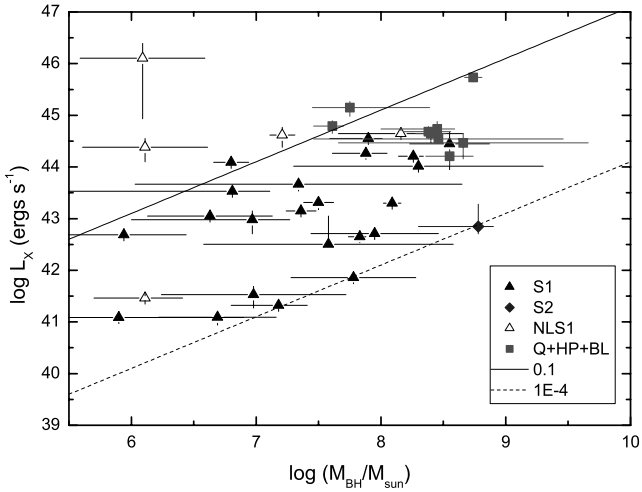


FIG. 4.—Soft X-ray luminosity vs. black hole masses. The solid line shows $L_{\rm X} = 0.1L_{\rm Edd}$, and the dashed line shows $L_{\rm X} = 10^{-4}L_{\rm Edd}$.

consistent with the results from the L_X-Δt diagram (see Fig. 3).

3.3. *Sizes of the X-Ray Radiation Regions*

Under unified model schemes, an accretion disk surrounds the central massive black hole in an AGN. There are two instabilities, thermal and viscous, usually occurring in accretion disks. However, the rapid variability in X-rays cannot arise from viscous instability because the viscous timescale is too long (Mushotzky et al. 1993). The timescale of thermal instability in accretion disks (Frank, King, & Raine 1992, p. 98) is

$$t_{\rm th} \sim \frac{1}{\alpha \Omega_{\rm K}} , \tag{8}$$

where α is a parameter in the standard thin accretion disk and $\Omega_{\rm K} = (GM/R^3)^{1/2}$ is the Keplerian angular velocity in an orbit of radius R surrounding a central black hole with a mass of M.

Assuming the exponential timescale is approximately equal to the thermal timescale, we can obtain the size of radiation region, R_X, as

$$\frac{R_X}{R_g} = \left(\frac{\alpha}{\sqrt{2}} \frac{c \Delta t_e}{R_g} \right)^{2/3} , \tag{9}$$

where $R_g = 2GM/c^2$ is the Schwarzschild radius and $\alpha = 1$ is adopted.

Taking the above estimated black hole masses and exponential timescales, we can obtain the ratios of the size of the X-ray radiation region to the Schwarzschild radius, which are listed in column (7) of Table 1. The R_X/R_g distribution is $\langle \log(R_X/R_g) \rangle = 0.97 \pm 0.12$, with a standard deviation of 0.75. We plot R_X/R_g versus $M_{\rm BH}$ in Figure 5. A simple least-squares linear regression (Press 1992) gives

$$\log \left(\frac{R_X}{R_g} \right) = 4.52 \pm 0.92 + (-0.47 \pm 0.12) \log \left(\frac{M_{\rm BH}}{M_\odot} \right) ;$$

with a Pearson correlation coefficient of $R = 0.54$ corresponding to a probability of $P < 0.000431$ that the correlation is caused by a random factor. The error of R_X/R_g is estimated from the errors of the exponential timescale and the black hole mass. The sizes of the radiation regions of all the AGNs are larger than the so-called last stable radius $3R_g$, if we consider the errors of the calculated sizes.

3.4. *Accretion Rates*

The accretion rate $\dot{M}$ can be derived from the relation $L_X \simeq GM_{\rm BH}\dot{M}/R_X$:

$$\dot{M} = \frac{2L_X(R_X/R_g)}{c^2} , \tag{10}$$

where L_X is the soft X-ray luminosity in the 0.1–2.4 keV band, G is the gravitational constant, and R_X is the size of the X-ray radiation region. Using R_X/R_g and L_X, accretion rates for 37 AGNs are obtained from equation (10), which are listed in column (6) of Table 1. The $\dot{M}$ distribution is $\langle \log(\dot{M}) \rangle = -1.50 \pm 0.23$, with a standard deviation of 1.42. In Figure 6 we show the accretion rates ($\dot{M}$) versus black hole masses ($M_{\rm BH}$). The accretion rates of most of the AGNs are (100–0.01)$\dot{M}_{\rm Edd}$, where $\dot{M}_{\rm Edd} = 0.2(M/10^8\ M_\odot)\ M_\odot\ {\rm yr}^{-1}$.

We plot L_X versus $\dot{M}$ in Figure 7 using $L_X = \zeta \dot{M} c^2$, where ζ is the accretion efficiency. The solid line in Figure 7 shows $L_X = 0.1\dot{M}c^2$, and the dashed line shows $L_X = 0.001\dot{M}c^2$. Most AGNs are in the range of (0.1–0.001)ζ. Combining with equation (10), we can derive the accretion efficiency $\zeta = 1/(2R_X/R_g)$. From Figure 5 we find that the values of R_X/R_g in most AGNs are in the range of 5–500, which is consistent with the value of (0.1–0.001)ζ.

3.5. *The Compactness Parameter*

If the power-law spectra observed in AGNs in the X-ray extend to much higher energies, then pairs may be expected to be produced if the optical depth of the γ-ray photons for pair production exceeds unity. The condition is usually stated in terms of the compactness parameter (Done & Fabian 1989):

$$l = \frac{\sigma_{\rm T}}{m_e c^3} \frac{L_X}{R_X} , \tag{11}$$

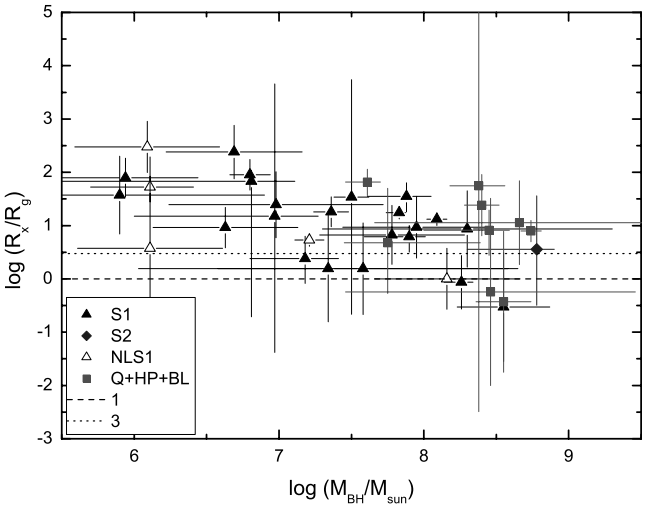


FIG. 5.—Plot of $\log(R_X/R_g)$ vs. $\log(M_{\rm BH})$. The dashed line shows $R_X/R_g = 1$, and the dotted line shows $R_X/R_g = 3$.

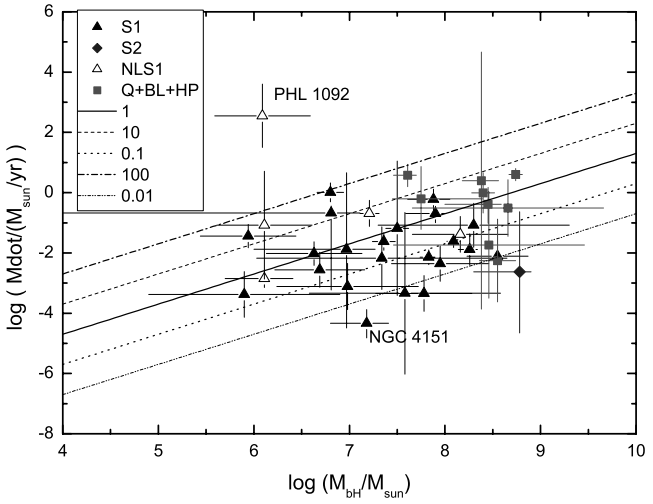


FIG. 6.—Plot of $\log(\dot{M})$ vs. $\log(M_{\rm BH})$, where $\dot{M} = \epsilon \dot{M}_{\rm Edd}$. The factor ϵ is 1, 10, 0.1, 100, and 0.01, respectively, for the solid line, dashed line, dotted line, dot-dashed line, and double-dot–dashed line.

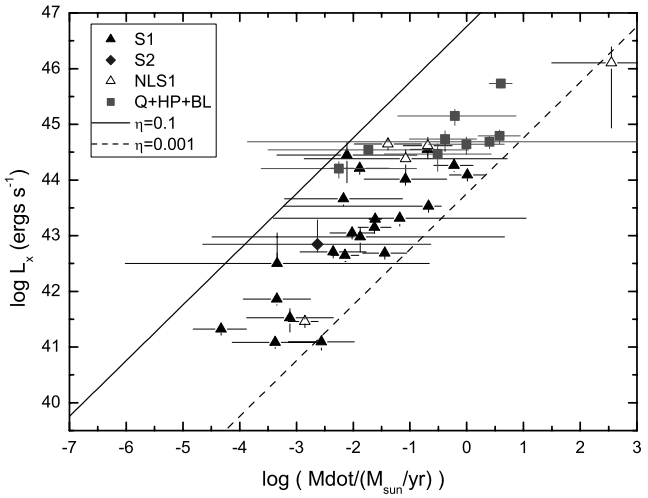


FIG. 7.—Plot of $\log(L_X)$ vs. $\log(\dot{M})$. The solid line and dashed line show $L_X = \zeta \dot{M} c^2$ with $\zeta = 0.1$ and 0.001, respectively.

where L_X is the luminosity produced in the region of R_X, m_e is the mass of the electron, and σ_T is the Thomson cross section. The values of the compactness parameters are listed in column (8) of Table 1. If $l > 20\pi$, the source has unity optical depth in the X-ray for γ-ray absorption at about 1 MeV, and a significant fraction of the source luminosity can then pass through electron-positron pairs. The distribution of the compactness parameter is $\langle \log(l) \rangle = 0.90 \pm 0.20$, with a standard deviation of 1.23. We plot the compactness parameter versus R_X/R_g in Figure 8. A simple least-squares linear regression (Press 1992) gives

$$\log(l) = (1.70 \pm 0.29) + (-0.85 \pm 0.25) \log\left(\frac{R_X}{R_g}\right)$$

(excluding PHL 1092; $R = -0.50$, $P = 0.00168$). Those AGNs with a smaller R_X/R_g appear to have a larger compactness parameter. From Figure 8 we can find that several AGNs have $l > 20\pi$, while several other AGNs have $l < 0.1$, which is consistent with the results of Done & Fabian (1989).

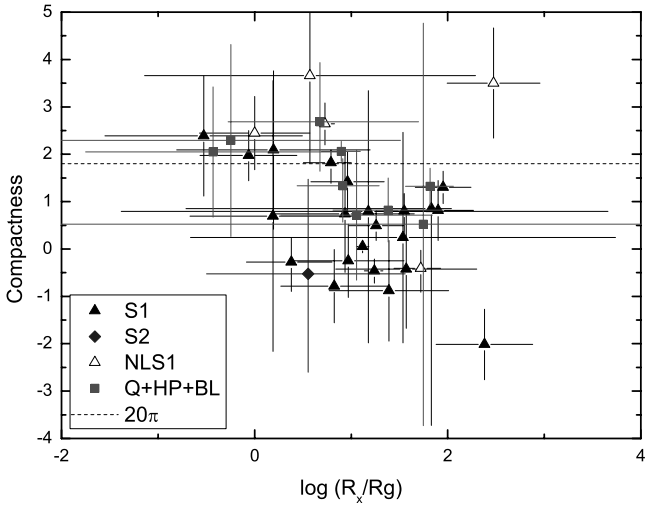


FIG. 8.—The log of the compactness parameter l vs. $\log(R_X/R_g)$. The dashed line shows $l = 20\pi$.

4. THE SIZES OF BROAD-LINE REGIONS

Broad emission lines are one of the dominant features of the spectra of AGNs. BLRs play a particularly important role in our understanding of AGNs by virtue of their proximity to the central source. With reverberation mapping techniques, the sizes of the BLRs can be obtained through the study of correlated variations of the lines and continuum fluxes (Peterson 1993). The BLR sizes for 17 S1s (Wandel, Peterson, & Malkan 1999) and for 17 PG QSOs (Kaspi et al. 2000) have been recently obtained. In Table 2 we list 12 AGNs with available BLR sizes and the calculated accretion rates. Here we adopted 3 lt-days as the error of the BLR size of NGC 3516, which is not given in Ho (1998). The errors of the BLR sizes of the other 11 AGNs are from Kaspi et al. (2000).

We assume that the gravitational instability of the standard thin disk at large radius leads to the formation of BLRs (Bian & Zhao 2002). The criterion is $Q = \Omega_K^2/\pi G\rho \leq 1$ (Goldreich & Lynden-Bell 1965), where Ω_K is the Keplerian angular velocity at R away from the central black hole $(GM/R^3)^{1/2}$, M is the black hole mass, and ρ is the local mass density. We adopted the solutions of ρ for the standard thin disk from Shakura & Sunyaev (1973), $\rho = 3.1 \times 10^{-5} \alpha^{-7/10} \dot{M}_{26}^{11/20} M_8^{5/8} R_{14}^{-15/8} f^{11/5}$ g cm^{-3}, where α is the parameter of the standard α-disk, $f = [1 - (R/R_s)^{1/2}]^{1/4}$, $\dot{M}_{26} = \dot{M}/(10^{26}$ g s$^{-1})$, $M_8 = M/(10^8\ M_\odot)$, and $R_{14} = R/(10^{14}$ cm). The values $f = 1$ and $\alpha = 1$ are adopted in AGNs. We can obtain the sizes of the BLRs if we know the central black hole masses and accretion rates:

$$R_{14} = 880 \alpha^{28/45} Q^{-8/9} \dot{M}_{26}^{-22/45} M_8^{1/3} . \quad (12)$$

The BLR sizes of 12 AGNs are obtained from equation (12), which are listed in Table 2. The uncertainties of our calculated BLR sizes are estimated from errors of the black hole masses and accretion rates, considering $\frac{1}{4} \leq Q \leq 4$ (Goldreich & Lynden-Bell 1965).

Figure 9 shows that the calculated BLR sizes derived from equation (12) are consistent with the sizes from the reverberation mapping method. We have a χ^2 (Press 1992)

TABLE 2
BLR SIZE OF 12 AGNs

Name (1)	R_{BLR} (10^{14} cm) (2)	$\log(M/M_\odot)$ (3)	$\log \dot{M}$ ($M_\odot$ yr^{-1}) (4)	R_{cal} (10^{14} cm) (5)
F9	$422.5^{+85.5}_{-197}$	$7.90^{+0.11}_{-0.31}$	$-0.69^{+0.24}_{-0.31}$	$815.0^{+1979.6}_{-577.3}$
NGC 3783	$116.7^{+93.3}_{-80.4}$	$6.97^{+0.30}_{-0.97}$	$-1.87^{+2.54}_{-2.61}$	$399.2^{+969.6}_{-282.8}$
Ark 120	$969.4^{+132.2}_{-163.3}$	$8.26^{+0.08}_{-0.12}$	$-1.89^{+0.52}_{-0.52}$	$1074.4^{+2609.6}_{-761.0}$
3C 273	$10031^{+1503.4}_{-1296}$	$8.74^{+0.07}_{-0.07}$	$0.60^{+0.20}_{-0.20}$	$1552.9^{+3772.0}_{-1100.0}$
PG 1211	$2617.9^{+596.2}_{-751.7}$	$7.61^{+0.09}_{-0.15}$	$0.58^{+0.37}_{-0.38}$	$652.4^{+1584.5}_{-462.1}$
Mrk 335	$425.1^{+132.2}_{-82.9}$	$6.80^{+0.14}_{-0.14}$	$0.01^{+0.31}_{-0.31}$	$350.3^{+851.0}_{-248.2}$
Ton 1542	$1296^{+622.1}_{-596.2}$	$8.74^{+0.17}_{-0.27}$	$-0.22^{+0.33}_{-0.36}$	$1552.9^{+3772.0}_{-1100.0}$
NGC 5548	$549.5^{+62.2}_{-18.1}$	$8.09^{+0.07}_{-0.07}$	$-1.61^{+0.065}_{-0.065}$	$942.9^{+2290.4}_{-667.9}$
NGC 4151	$77.8^{+46.7}_{-36.3}$	$7.18^{+0.23}_{-0.38}$	$-4.33^{+0.445}_{-0.49}$	$469.0^{+1139.1}_{-332}$
NGC 4051	$168.5^{+171.1}_{-106.3}$	$6.11^{+0.30}_{-0.41}$	$-2.85^{+0.23}_{-0.30}$	$206.3^{+501.1}_{-146}$
3C 390.3	$593.6^{+163.3}_{-207.4}$	$7.36^{+0.10}_{-0.10}$	$-1.62^{+0.29}_{-0.29}$	$1321.7^{+3210.5}_{-936.3}$
NGC 3516	$181.4^{+77.8}_{-77.8}$	$8.53^{+0.12}_{-0.21}$	$0.81^{+0.21}_{-0.66}$	$538.5^{+1307.9}_{-381.4}$

NOTES.—Col. (1): Name. Col. (2): BLR sizes from the reverberation mapping method (Kaspi et al. 2000). Col. (3): Central black hole masses (Kaspi et al. 2000). Col. (4): Calculated accretion rate. Col. (5): Calculated BLR size.

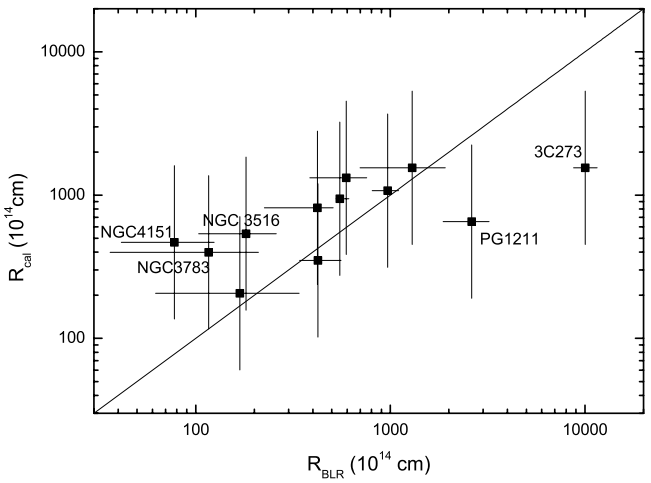


FIG. 9.—Plot of $\log(R_{\rm cal})$ vs. $\log(R_{\rm BLR})$. The solid line shows 1 : 1.

test of $\log R_{\rm BLR}$ to show whether our calculated BLR sizes are consistent with those from the reverberation mapping method. The χ^2 and probability are 0.933 and 99.996% for the 12 AGNs.

5. SUMMARY

We use the exponential timescale to characterize the soft X-ray variabilities of AGNs with obvious exponentially increasing or decreasing patterns in their light curves and obtain timescales for 65 AGNs. The exponential timescale is suitable for analyzing X-ray variability, especially for the data with larger time gaps such as *ROSAT* data. The exponential timescales can provide good upper limits for the central black hole masses and the sizes of the X-ray radiation regions. From the relationship of $L_{\rm X}$ and Δt_e, we can reject bremsstrahlung as the primary radiation source for most AGNs here. Many AGNs have very efficient engines. There is no explicitly grouped distribution in the $\dot{M}$-M diagram for different kinds of AGNs. This means that, under the same soft X-ray luminosity, the central mass or radiation region compared with the Schwarzschild radius varies from one AGN to another.

Using the recent mass estimates of central black holes and the exponential timescales of AGNs from *ROSAT*/PSPC pointing data and the sizes of X-ray radiation regions, the accretion rate and the compactness parameter of 37 AGNs are obtained. We use the calculated accretion rates to calculate the radii of gravitational instability for 12 among 37 AGNs, which is consistent with the BLR sizes from the reverberation mapping method. This provides further evidence for gravitational instability leading to the formation of BLRs.

We thank Keliang Huang for useful discussions and the anonymous referee for valuable comments. We thank Helmut Abt for reading our manuscript. This work was supported by the Chinese Natural Science Foundation (grant 10273007) and the NSF of the Jiangsu Provincial Education Department.

REFERENCES

Barr, P., & Mushotzky, R. F. 1986, Nature, 320, 421
Bian, W., & Zhao, Y. 2002, A&A, 395, 465
Czerny, B., Nikolajuk, M., Piasecki, M., & Kuraszkiewicz, J. 2001, MNRAS, 325, 865
Done, C., & Fabian, A. C. 1989, MNRAS, 240, 81
Edelson, R., & Nandra, K. 1999, ApJ, 514, 682
Fabian, A. C. 1979, Proc. R. Soc. London A, 266, 449
———. 1992, in Frontiers of X-Ray Astronomy, ed. Y. Tananka & K. Koyama (Tokyo: Universal Academy), 603
Falomo, R., Kotilainen, J. K., & Treves, A. 2002, ApJ, 569, L35
Ferrarese, L., Pogge, R. W., Peterson, B. M., Merritt, D., Wandel, A., & Joseph, C. L. 2001, ApJ, 555, L79
Frank, J., King, A. R., & Raine, D. J. 1992, Accretion Power in Astrophysics (New York: Cambridge Univ. Press)
Goldreich, P., & Lynden-Bell, D. 1965, MNRAS, 130, 97
Green, A. R., McHardy, I. M., & Lehto, H. J. 1993, MNRAS, 265, 664
Ho, L. C. 1998, in Observational Evidence for Black Holes in the Universe, ed. S. K. Chakrabarti (Dordrecht: Kluwer), 157
Kaspi, S., Smith, P. S., Netzer, H., Maoz, D., Jannuzi, B. T., & Giveon, U. 2000, ApJ, 533, 631
Kormendy, J., & Gebhardt, K. 2001, in AIP Conf. Proc. 586, 20th Texas Symp. on Relativistic Astrophysics, ed. H. Martel & J. C. Wheeler (New York: AIP), 363
Li, T. P. 2001, Chinese J. Astron. & Astrophys., 1, 313
Mathur, S., Kuraszkiewicz, J., & Czerny, B. 2001, NewA, 6, 321
McHardy, I. M. 1988, Mem. Soc. Astron. Italiana, 59, 239
Merritt, D., & Ferrarese, L. 2001, ApJ, 547, 140
Mushotzky, R. F., Done, C., & Pounds, K. A. 1993, ARA&A, 31, 717
Nandra, K., George, I. M., Mushotzky, R. F., Turner, T. J., & Yaqoob, T. 1997, ApJ, 476, 70
Nelson, C. H. 2000, ApJ, 544, L91
Nelson, C. H., & Whittle, M. 1995, ApJS, 99, 67
Otazu, X., Ribó, M., Peracaula, M., Paredes, J. M., & Nuñez, J. 2002, MNRAS, 333, 365
Padovani, P., Burg, R., & Edelson, R. A. 1990, ApJ, 353, 438
Padovani, P., & Rafanelli, P. 1988, A&A, 205, 53
Papadakis, I., & McHardy, I. 1995, MNRAS, 273, 923
Peterson, B. M. 1993, PASP, 105, 247
Pounds, K., Edelson, R., Markowitz, A., & Vaughan, S. 2001, ApJ, 550, L15
Press, W. H., Teukolsky, S. A., Vetterling, W. T., & Flannery, B. P. 1992, Numerical Recipes in FORTRAN: The Art of Scientific Computing (New York: Cambridge Univ. Press)
Shakura, N. I., & Sunyaev, R. A. 1973, A&A, 24, 337
Tremaine, S., et al. 2002, ApJ, 574, 740
Uttley, P., McHardy, I. M., & Papadakis, I. E. 2002, MNRAS, 332, 231
Véron-Cetty, M. P., & Véron, P. 2001, A&A, 374, 92
Vestergaard, M. 2002, ApJ, 571, 733
Wandel, A., Peterson, B. M., & Malkan, M. A. 1999, ApJ, 526, 579
Wang, T. G., & Lu, Y. J. 2001, A&A, 377, 52
Zhao, Y., & Fink, H. 1996, in Proc. Röntgenstrahlung from the Universe, ed. H. U. Zimmermann, J. Trümper, & H. Yorke (MPE Rep. 263; Garching: MPI), 535